Case Studies in Construction Materials 19 (2023) e02355

Contents lists available at ScienceDirect

Case Studies in Construction Materials

journal homepage: www.elsevier.com/locate/cscm

Case study

Experimental characterisation of hygrothermal properties of a 3D printed cementitious mortar

Sofia Pessoa [a], Manuel Jesus [a], Ana S. Guimarães [a], Sandra S. Lucas [b,*], Nuno Simões [c,d]

[a] CONSTRUCT-LFC, Faculty of Engineering (FEUP), University of Porto, Portugal
[b] Department of the Built Environment, Eindhoven University of Technology, Netherlands
[c] University of Coimbra, CERIS, Department of Civil Engineering, Coimbra, Portugal
[d] Institute for Research and Technological Development in Construction (Itecons), Energy, Environmental and Sustainability, Portugal

ARTICLE INFO

Keywords:
3D printing
Hygrothermal characterisation
Thermal conductivity
Water vapour permeability
Capillary water absorption
Sorption isotherm
Cementitious mortar

ABSTRACT

3D printing (3DP) presents great potential for automation, sustainability, and quality control in the construction sector. However, research on 3DP in Construction has been carried out primarily from a structural standpoint, and information on the thermal performance, comfort and energy efficiency of these solutions remains very limited. Given the importance of assessing how printed walls perform when subjected to hygrothermal solicitations, this work experimentally analyses a cement-based mortar specially developed for 3DP. An extensive laboratory campaign was carried out, and the following set of physical, hygric and thermal properties was obtained: the dry bulk density, saturation moisture content, specific heat capacity, porosity, water absorption due to capillary action, water vapour permeability, thermal conductivity (dry and moisture-dependent), and the sorption isotherm. The results show that the 3D printed cement-based mortar, which presents a dry density of 2060 kg/m^3 and a thermal conductivity of 1.33 W/(m K), has a hygrothermal performance comparable to that of traditional cast concrete. This indicates that additional thermal insulation materials are required for appropriate thermal performance through the building envelope. Moreover, this detailed hygrothermal characterisation is suitable for design purposes, allowing the use of the obtained properties in future numerical simulations, important for studying the hygrothermal performance of printed building elements in service.

1. Introduction

The high fragmentation of the construction industry often represents a setback to its development and innovation. Motivated to adapt and revolutionise its approaches while becoming more sustainable and efficient, the industry recognises the potential for productivity, innovation and technological integration in 3D printing (3DP).

The main challenge for the full-scale implementation of 3DP lies in developing extrudable mixtures compatible with the printing and pumping systems. While cement-based materials are attractive for producing structural mortars for 3DP, concrete has a significant impact on global carbon emissions. Moreover, ensuring their pumpability, extrudability, and buildability demands enhanced control over rheological properties compared to traditional casted concrete. Thus, active areas of research include the study of low-carbon

* Corresponding author.
E-mail address: s.s.d.o.lucas@tue.nl (S.S. Lucas).

https://doi.org/10.1016/j.cscm.2023.e02355
Received 26 May 2023; Received in revised form 20 July 2023; Accepted 27 July 2023
Available online 29 July 2023

binders alternative to Portland cement, such as geopolymers [1,2], the replacement of mineral aggregates by waste materials [3] and the impact of nano-additives on shape retention and mechanical performance [4]. However, Portland cement remains the main component in most mix compositions [5]. Therefore, despite the promising advancements of 3DP implementation in Construction, addressing critical challenges related to scalability, commercialisation, and sustainability of 3D printable cement-based materials remains imperative.

Fresh-state and structural properties have been the focus of material development [6,7]. Previous research ([8,9]) has demonstrated that fibre reinforcement enhances the compressive and flexural strength, ductility, and shrinkage mitigation of structures printed using cement-based mixtures. However, in a similar way to traditional cast concrete structures, 3D printed buildings also need to create a desired indoor thermal environment. Thus, the need for research into thermal performance, energy efficiency, and moisture transport phenomena increases as 3DP techniques become more widely used in Construction applications.

The façade is one of the critical elements for adequate thermal comfort [10,11]. Poor envelope insulation can lead to energy losses or gains during the use phase [12,13], resulting in the need for expensive heating/cooling systems to preserve the appropriate temperature inside the building. However, there are few studies on the application of thermal insulation to printed building elements. Sun *et al.* [14] conducted a thermographic examination and heat transfer monitoring of a 3D printed concrete building prototype without insulation. The results show a high risk of heat loss and a wall U-value of 2.27 $W/(m^2 \bullet K)$. Moreover, the authors state that if the thermal properties of the tested 3D printed concrete envelop are not improved, an insulation system will be required.

The need for more specific, automatable solutions for thermal insulation is a topic that needs to be addressed. Some possibilities could be the placement of dry or loose insulation materials in the cavities between structural layers, the extrusion of a thermal mortar at the same time and side-by-side with a structural mortar, or the development and formulation of new compositions with the addition of low thermal conductivity additives [15]. The most researched approach has been to formulate new mixtures by incorporating cork [16], pre-wetted expanded thermoplastic microspheres [17], expanded polystyrene beads [18], replacing sand with recycled rubber powder [19], and producing foam concretes [20] or geopolymer foams [21]. Designing and optimising new printable mortars is a significant challenge for the future implementation of 3DP in the construction industry [22]. However, considering the difficulty of developing a single material capable of simultaneously satisfying the hygrothermal and structural demands to which a building is subjected, it is expected that it will be necessary to combine materials with different purposes in the immediate future.

To date, thermal insulation in printed buildings has been achieved with commercial materials applied in the cavities of hollow walls. This is the case of the first house printed within the Milestone project, where polyurethane foam was placed in these wall cavities [23]. The 94 m^2 one-story house meets all the building requirements of the Netherlands and consists of 24 concrete elements, which were printed off-site, transported and assembled at the construction site [24].

The thermal performance of entire buildings and construction systems, as is the case of multilayer walls, can be predicted through numerical simulation software that allows the evaluation of different strategies and scenarios for their optimisation. These tools can be used to study, among others, the occurrence of thermal bridges in the connection between different printed elements and the risk of pathologies, such as condensation on the interior surface of the wall. However, obtaining reliable simulation results depends on several parameters required by the software, among which is the accurate hygrothermal properties of the materials. Detailed material characterisation has been carried out in other families of products during the research phase of developing new solutions. A study by Posani *et al.* [25] provided a detailed characterisation of insulation solutions based on thermal mortars, and Maaroufi *et al.* [26] presented a complete experimental characterisation of a recycled expanded polystyrene mortar to help predict the hygrothermal and mechanical behaviour of the material under analysis.

In this work, an analysis of the thermal and hygric properties of the cement-based mortar used to additively manufacture the first 3D printed house from project Milestone was carried out. This study responds to an existing research gap in the design of 3D printed wall solutions related to the lack of reliable material properties of printed concrete, in particular hygrothermal properties. A promising and mostly unexplored area of research on these systems' multifunctionality is the combined study of the material and its hygrothermal properties. Moreover, this experimental characterisation provides an accurate and in-depth database for future sensitivity studies of 3D printed wall systems using hygrothermal simulation software.

2. Material, printing process and specimen preparation

Finding a mortar composition for 3DP lies in several conflicting factors. The mixture must exhibit sufficient fluidity to prevent the occurrence of blockages when pumped, a characteristic commonly referred to as extrudability. Nevertheless, it is also required that the mixture has adequate stiffness to allow for good buildability, shape retention and adequate bonding between successive layers immediately after extrusion. Therefore, the demand to develop a cementitious mixture for 3DP is a function of both pumpability, extrudability and buildability requirements.

Mortar properties depend on the binders and aggregates used and their respective proportions. Thus, specific properties can be obtained by the type of aggregates, adjuvants and additives used. The material studied in this research, Weber 3D 145–2, is a factory-produced dry mortar developed by Saint-Gobain Weber Beamix, especially for 3DP. It has a composition characteristic of a mortar (maximum particle size of 1 mm) associated with a mechanical performance similar to that of concrete (compressive strength class of C35/45) [27]. Wolfs *et al.* [28] evaluated its hardened properties, and the results showed a flexural tensile strength of 4.29 MPa, a tensile splitting strength of 3.68 MPa and a compressive strength of 28.51 MPa for an interlayer interval time equal to 15 s for all specimens. The constituent that sets it apart from traditional concrete is the coarse aggregate, which is not incorporated to prevent clogging of the pumping and extrusion systems. Its composition is presented below [29]:

- Portland cement CEM I 52.5 R;
- Siliceous aggregate;
- Limestone filler and specific additives for easier pumpability;
- Polypropylene fibres to minimise the occurrence of fissures caused by early drying;
- Rheology modifiers to resemble the behaviour of fresh mortar.

The 3DP process begins with drawing a 3D model of the design in modelling software, such as Rhino. The 3D model is exported to an STL file format, a standard file format that contains information regarding the surface geometry of the 3D object. Then, a slicing software decomposes the model into transversal layers, resulting in a series of 2D contour lines, which, together with further provided data on printing parameters, such as printing speed and layer height, are processed to generate control commands via g-code, the machine language for the positioning of the extrusion nozzle.

Using an M-Tec Duomix 2000 mixer-pump monitored by a numerical control unit, the mixture is pumped to the printer head through a hose. A filament of mortar is then deposited by the extrusion nozzle at the selected location at a certain speed and angle [29]. The specimens were printed continuously by a 3D gantry printer (see Fig. 1a). All printed objects were cut into specimens with the appropriate dimensions for the experimental work, as shown in Fig. 1b and c.

Different specimens were considered to evaluate the hygrothermal properties of the hardened material under study. The number of test specimens and their dimensions, defined according to the specifications of the standards followed, are identified in Table 1.

The specimens were selected to represent the material, present the most regular shape possible with constant cross-section, have a thickness equal to the thickness of the original product, as well as surfaces free of irregularities. To define the size of the specimens, it was necessary to consider the diameter of the extrusion nozzle used, which fixed the thickness of the specimens at 40 mm. The determination of the printer head speed and pump pressure resulted from a sensitivity test program.

3. Standards and methods

In a progressive approach towards the scalability and commercial adoption of 3D Construction Printing (3DCP), an official committee, designated as JG80, was established in early 2021 under ISO/TC 261-ASTM F 42 (WG2) to set standards and quality requirements for additive manufacturing in building and construction (structural and infrastructure elements) [30]. However, no specific Eurocode is currently available for mixtures developed to be 3D printed. Therefore, considering that the material under study is a resistant mortar (not containing larger aggregates), after studying both concrete and rendering mortar standards, it was decided to adopt the mortar standards.

Table 2 provides the complete list of material properties and corresponding test standards in the experimental campaign. The selection of the experimental tests aimed to address the different aspects relevant to evaluating the hygrothermal performance of the material under study, namely physical, thermal, and hygroscopic properties. All the selected test standards considered the suitability of the material under study for the corresponding procedure.

The European standard EN 998 (CEN 2017) [39] addresses rendering/plastering mortars, presenting its final performance requirements and referencing standards to determine performance properties. Since the material under study is in its hardened state, the European standard refers to EN 1015–10:1999 [31] for determining the dry bulk density. Although there is an amendment (A1:2006) to the mentioned standard, this modification takes the volume of the hardened specimen as the volume of the mould. Thus, considering that the specimens were printed and not prepared using a mould, the method described in the 1999 version is more appropriate for determining the volume of irregular shapes, see Fig. 1b and c, since it proposes the water displacement method.

Regarding the determination of the saturation moisture content, the test was performed following the principle described in EN 13755:2008 [32], which considers total immersion at atmospheric pressure. The evaluation of porosity followed ISO 15901–1:2016 [33] via the mercury porosimetry method for pores in the approximate diameter range of 0.002 μm to 400 μm. While for determining the specific heat capacity, the test described in ASTM E1269–11:2018 [34], which applies the differential scanning calorimetry method, was adopted.

An extensive campaign of experimental tests was carried out. The thermal conductivity coefficient was determined by the guarded hot plate method, following the test procedures defined in EN 12664:2001 [35], adequate to dry and moist products of medium and

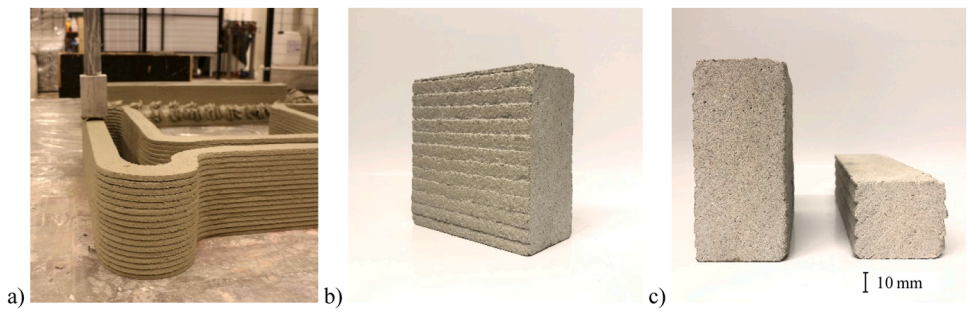

Fig. 1. 3D printing process (a), an example of 3D printed specimens (b), and irregularities of the specimen's surfaces (c).

Table 1
Specimens' dimensions and quantity according to the material properties tested.

Material properties	Specimens		
	Dimensions (mm)	Quantity	Identification
Dry bulk density	160 × 40 × 40	6	D1 to D6
Saturation moisture content	Same specimens as the dry bulk density test	6	D1 to D6
Porosity	Fragments from another test	-	-
Specific heat capacity	Fragments from another test	-	HC1 to HC3
Thermal conductivity	300 × 300 × 40 (*Holometrix GHP-300*)	3	TC1 to TC3
(dry and as a function of moisture content)	150 × 150 × 40 (*Single Specimen λ-Meter EP500e*)	6	TC4 to TC9
Water absorption due to capillary action	40 × 40 × 100	5	CA1 to CA5
	100 × 100 × 40	5	CA6 to CA10
Water vapour permeability	210 × 210 × 40	3	VP1 to VP3
Sorption isotherm	100 × 100 × 40	5	SI1 to SI5

Table 2
Material properties and corresponding test methods.

Material properties	Symbol, unit	Test standard	Method
Dry bulk density	ρ, kg/m^3	EN 1015–10:1999 [31]	Volume by means of displacement
Saturation moisture content	w_{sat}, % A_b, %	EN 13755:2008 [32]	Total immersion at atmospheric pressure
Porosity	ε, %	ISO 15901–1:2016 [33]	Mercury porosimetry
Specific heat capacity	c_p, J/(kg • K)	ASTM E1269–11:2018 [34]	Differential scanning calorimetry
Thermal conductivity (dry and as a function of moisture content)	λ, W/(m • K)	EN 12664:2001 [35]	Guarded hot-plate
Water absorption due to capillary action	A_w, $kg/(m^2s^{0.5})$	ISO 15148:2002 [36]	One-direction absorption by partial immersion
Water vapor permeability	δ_p, kg/(m • s • Pa)	ISO 12572:2016 [37]	Wet cup
Sorption isotherm	w(φ)	ISO 12571:2013 [38]	Climatic chamber

low thermal resistance.

The coefficient of water absorption by capillarity was determined according to ISO 15148:2002 [36] by partial immersion of a specimen with one surface in contact with water without a temperature gradient. Water vapour transmission properties were determined as specified in ISO 12572:2016 [37] by a method based on cup tests containing either a desiccant (dry cup) or an aqueous saturated solution (wet cup). Based on ISO 12571:2013 [38], the climatic chamber method was used to determine the hygroscopic sorption properties.

4. Test procedures

4.1. Dry bulk density

The dry bulk density, ρ, depends on the percentage of voids in the material, is expressed in kg/m^3, and was assessed in compliance with EN 1015–10:1999 [31]. The specimens were oven-dried at 70°C ± 5°Cuntil reaching a constant mass (measures at each 24 h) and weighed with a precision of ± 0.01 g. The test specimens were then immersed in water under the procedure in EN 13755:2008 [32]: at time t_0, tap water was added until half the height of the specimens; at time t_0 + (60 ± 5) min, tap water was added until the water level reached three-quarters of the specimens' height; and at time t_0 + (120 ± 5) min, until the specimens were completely immersed to a depth of (25 ± 5) mm (Fig. 2a). When no further increase in mass was observed, the saturated mass values were registered.

Since the specimens produced by the 3DP manufacturing technology have irregular shapes (due to the layering effect), the volume was calculated using the water displacement method reflected in Eq. (1). For the hydrostatic weighing (Fig. 2b), each saturated specimen was placed in a stirrup fully immersed in water, hanging from a weighing instrument. The ρ was determined through the ratio of dry mass to submerged volume in a saturated state, as given in Eq. (2) where V corresponds to the volume of the specimen, in m^3, ρ_w to the water density at 20°C, taken as 998 kg/m^3, m_0 to the oven-dry mass, m_s to the saturated mass, and m_h to the saturated immersed mass, in kg.

$$V = \frac{m_s - m_h}{\rho_w} \tag{1}$$

$$\rho = \frac{m_0}{V} = \frac{m_0}{m_s - m_h} \times \rho_w \tag{2}$$

Fig. 2. Experimental campaign: determination of dry bulk density and saturation moisture content (a, b), specific heat capacity (c), thermal conductivity (d, e), water absorption due to capillary action (f, g), water vapour permeability (h), and sorption isotherm (i).

4.2. Saturation moisture content

The saturation moisture content, w_{sat}, expressed in kg/m^3, was experimentally determined as described: the specimens were dried at a temperature of 70℃ ± 5℃ and weighed with a precision of ± 0.01 g; then, the specimens were immersed in water for a period of time such that their mass stabilisation was verified through successive weighings; when equilibrium was reached, the specimens were removed from the water, wiped with an absorbent cloth and weighed.

The w_{sat} values were obtained through Eq. (3), in compliance with ISO 12570:2000 [40], and the water absorption at atmospheric pressure, expressed as a percentage, A_b, of each specimen was calculated, following the standard EN 13755:2008 [32], by Eq. (4), where V corresponds to the volume of the specimen, in m^3, m_0 to the mass of the test specimen after drying in the oven and m_s to the constant mass reached after immersion in water, in kg.

$$w_{sat} = \frac{m_s - m_0}{V} \tag{3}$$

$$A_b = \frac{m_s - m_0}{m_0} \bullet 100 \tag{4}$$

4.3. Porosity

Defined as the ratio of the volume of the accessible pores and voids to the volume of the solid material, porosity, ε, was determined according to ISO 15901–1:2016 [33]. A mercury porosimetry test method in which the pores of the solid material are filled with mercury under pressure was followed.

An *Autopore IV 9500* porosimeter from *Micrometrics* was used, with the capacity to perform two sequential measurements: a low-pressure measurement, capable of reaching a pressure of 0.2 MPa (30 psi), and a high-pressure measurement that reaches the

maximum capacity of the porosimeter, of around 400 MPa (60 000 psi).

The test was carried out on a specimen taken from a specimen representative of the material, with a volume in a range between 1 cm^3 and 15 cm^3. The test piece was placed in a specimen holder consisting of a capillary tube with a uniform cross-section through which the specimen can be evacuated and the mercury can enter. This tube was connected to a larger diameter reservoir where the specimen was placed. The specimen holder was sealed by applying a thin layer of a high-viscosity lubricant to the contact area between the holder and its lid.

The mass of the specimen holder, m_{SH}, and the final mass of the specimen holder and specimen assembly after sealing, m_{SH+S}, are determined. The final mass of the specimen, m_S, is the difference between m_{SH+S} and m_{SH}. After sealing, a spacer is placed on the specimen holder and introduced into the equipment. An evacuation procedure, consisting of removing most of the vapours and gases trapped in the specimen, is carried out before filling the specimen holder with mercury at a filling pressure below 5 kPa.

The low-pressure test procedure consists in introducing a dry non-reactive gas (usually nitrogen) into the evacuated specimen holder in a controlled manner to increase the pressure either in stages, continuously or at pressurisation intervals to obtain equilibrium conditions suitable for the intrusion of mercury into the pores and to ensure an accuracy corresponding to the pore sizes of interest. When the maximum pressure is reached, it should decrease to atmospheric pressure, and the specimen holder should be transferred to the high-pressure unit. After the described process, the assembly mass was determined, $m_{SH+S+Hg}$.

For the high-pressure test procedure, the specimen holder is transferred to the high-pressure unit so that the total length of the capillary is available. The pressure in the system increases until the final pressure recorded in the low-pressure stage is reached. The volume of mercury introduced for this pressure is recorded so that the subsequent volume to be introduced is calculated from this initial volume. The pressure via hydraulic fluid on the mercury increases in stages, either continuously (uninterrupted increase in pressure and time) or in steps (uniform and regular increase, in unity, of the pressure-time interval), or stages (non-uniform increases in both pressure and time, in numbered intervals), by the equilibrium conditions of the mercury entering the pores. Consequently, mercury is pressed into the pore system, and the decreasing length of the mercury column is measured as a function of pressure. The values are recorded in the equipment's software. When the maximum pressure is reached, it decreases to atmospheric pressure in stages, steps, or continuously to determine the mercury extrusion curve. Eqs. (5) to (8), where V_B is the bulk volume and V_S the skeleton volume, allow the determination of the porosity.

$$V_{Hg} = \frac{m_{SH+S+Hg} - m_{SH+S}}{\rho_{Hg}} \tag{5}$$

$$V_B = V_{SH} - V_{Hg} \tag{6}$$

$$V_S = V_B - V_{Hg,max} \tag{7}$$

$$\varepsilon = \frac{V_B - V_S}{V_B} \bullet 100 \tag{8}$$

4.4. Specific heat capacity

The specific heat capacity is commonly designated by the symbol c_p, expressed in $J/(kg \bullet K)$, and was obtained by differential scanning calorimetry (DSC), following the ratio method. Per the procedures in ASTM E1269–11:2018 [34], the test involves heating the material in the specimen holder and an empty specimen holder of reference at a controlled rate, atmosphere, and over the temperature range of interest. Specimens with few milligrams were used; therefore, sampling was done by removing small portions of various parts of larger blocks, which were mixed to ensure the homogeneity and representativeness of the specimen. The specimens were placed in the specimen holder, weighed, and tested using the *NETZSCH DSC200F3* differential scanning calorimeter shown in Fig. 2c.

The equipment was calibrated using a set of standards for a wide range of temperatures and enthalpies. Readings were taken from the specimens under study and a representative sapphire standard. The test was performed at a heating rate of 20°/min, the sapphire standard was 49.93 mg and the same specimen holder was used to obtain the baseline, as well as the reference and specimen readings. The remaining parameters vary with temperature and were extracted directly from the thermograms. Considering the standard, all calculations were performed using the NETZSCH software associated with the DSC.

4.5. Thermal conductivity

The thermal conductivity, generally referred to as λ and was assessed both dry and depending on moisture content using the guarded hot plate method (ISO 8302:1991 [41]) following the procedure defined in EN 12664:2001 [35]. The following test conditions were defined:

- dry conditioning in a ventilated oven: 70 ± 5°C,
- humidity conditioning: (23 ± 2°C and 50 ± 5%) and (23 ± 2°C and 80 ± 5%),
- mean test temperature: 10°C, and
- temperature difference between plates: 10°C.

The mean test temperature, temperature difference, and the moisture contents selected were defined in conformity with the referenced standard. Moreover, after conditioning, the specimens were wrapped with a film impermeable to water vapour. The experimental tests were first performed using equipment designated as *Holometrix GHP-300,* where equal-sized, smooth-surfaced specimens were tested in parallel.

All specimens tested have average side dimensions of 300 mm and an average thickness of 28.7 mm. The test specimens were subjected to a temperature gradient due to the positioning of the cooling and heating plates, represented in Fig. 2d. Vermiculite insulation was placed laterally so that, after stabilisation of the system, a constant and unidirectional flow was obtained in the perpendicular direction to the test specimen faces. It should also be noted that this test is time-consuming and may lead to moisture migration inside the specimens.

The thermal conductivity was calculated using Eq. (9), in which 1 and 2 are referencing the two test specimens used, EI corresponding to the electrical power supplied to the main heater, in W, S to the surface area of the main heater, in m^2, d to the specimen thickness, in m, and ΔT to the differential temperature on both sides of the specimens.

$$\lambda = \frac{EI}{S}\frac{1}{\left(\frac{\Delta T}{d}\right)_1 + \left(\frac{\Delta T}{d}\right)_2} \tag{9}$$

Then, the experimental tests were also performed using the *Single Specimen λ-Meter EP500e* from *Lambda Mebtechnik GmbH Dresden*. In the equipment illustrated in Fig. 2e, in contrast to *Holometrix GHP-300*, the temperature measurements on both specimen surfaces are performed directly by the apparatus with sensors incorporated in the plates, ensuring high measurement accuracy.

This apparatus uses a single test specimen and automatically displays the conductivity values measured on the screen. During the test, the temperature on the upper surface (in contact with the heating unit) increases, while the temperature on the lower surface (in contact with the cooling unit) decreases. The energy supplied to the system is kept constant until constant heat flows are obtained. It is necessary to guarantee that the heat fluxes along the lateral cross-sections are null; therefore, an outer layer was placed to prevent humidity from entering the testing zone, thus preventing possible inaccuracies.

4.6. Water absorption due to capillary action

The water absorption by partial immersion of a material represents the mass of water absorbed per area of the material in contact with water due to the action of capillary suction forces. The coefficient of water absorption by capillarity is represented by A_w and is usually expressed in $kg/(m^2s^{0,5})$. The test, performed according to ISO 15148:2002 [36], consists in placing the lower surface of each specimen immersed in water 5 ± 2 mm above the highest point on the base of the specimen (Fig. 3) and measuring the variation in the mass of each specimen as a function of time.

Before testing, the sides of the specimens were waterproofed by applying a water-based, vapour-tight epoxy resin as a sealant. The specimens were conditioned at the temperature and relative humidity of the laboratory, 23 ± 2℃ and 50 ± 5%, until a constant mass was reached. Then, the initial masses of the specimens were recorded using a balance accurate to 0.01 g.

The experimental test starts when specimens are placed in contact with water (Fig. 2f and g). From that moment, specimens are weighed after 5, 10, 20 and 40 min, as well as after 1, 2, 4, 8 and 24 h from the beginning of the test. The water level was periodically checked to ensure it remained constant during the test period. Before each weighing, the water droplets adhering to the test specimen were absorbed with a dry cloth.

The mass variation, Δm_t, expressed in kg/m^2, was determined by Eq. (10), where A is the area of the face of the specimens, in m^2, m_i the initial mass, and m_t the mass at time t, in kg. In agreement with ISO 15148:2002 [36], the resulting graph for the mortar under study presented a curve, which in the standard is designated as type B (convex curve). As the method for calculating the water absorption coefficient, A_w, expressed in $kg/(m^2s^{0,5})$, depends on the shape of the resulting curve, this property was calculated according to Eq. (11).

$$\Delta m_t = \frac{m_t - m_i}{A} \tag{10}$$

$$A_{w,24} = \frac{\Delta m_{tf}}{\sqrt{86400}} \tag{11}$$

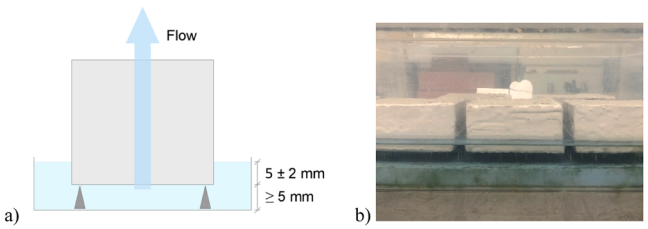

Fig. 3. Specimen placement for capillary absorption determination according to ISO 15148 [36]: schematic drawing (a), and a picture of the test procedure (b).

4.7. Water vapour permeability

The water vapour permeability of a homogeneous material, δ_p, is expressed in $kg/(m \bullet s \bullet Pa)$ and is defined as the water vapour flux diffusing through that material when its opposite faces are subjected to different partial vapour pressures. According to ISO 12572:2016 [37], the resistance to water vapour diffusion, μ (dimensionless), can also be calculated. The μ indicates how much greater the diffusion resistance of the material is compared to a layer of stationary air with the same thickness and at the same temperature.

A saturated aqueous solution of potassium nitrate (KNO_3, wet cup) was used to keep the indoor environment at 94% of relative humidity. Table 3 identifies the specimens under study and the test conditions selected according to the standard followed, ISO 12572:2016 [37].

The saturated aqueous solution was placed in metallic test cups to a height of 15 mm, followed by the specimens, as shown in the configuration illustrated in Fig. 4. The specimens and the cups were previously coated with aluminium foil tape to ensure the correct placement of the melted paraffin.

After placing the specimens in the cups, the void between the specimen and the cup was sealed with melted paraffin so that the vapour flow generated happens exclusively through the specimen's surface. The cups are tight to vapour diffusion and have a square cross-section, resulting in an exposed test specimen area of 0.039 m^2. An initial weighing was performed, and the cups with the specimens were placed in the *Vötsh VC 4034* climatic chamber under controlled temperature and relative humidity conditions (see Fig. 2h).

The test assemblies were weighed periodically, and the mass change rate, Δm_{12}, in kg/s, was determined by Eq. (12). The water vapour flow rate through the specimen, G, in kg/s, corresponds to the mean of five successive determinations of Δm_{12} for each test specimen. The test is completed when five consecutive values of the mass change rate are constant within a tolerance of 5% of the average of these values.

When the test specimens' edges overlap the cups' edges, a two-dimensional vapour flow can be caused, leading to an over-estimation of the permeance. To account for this effect, the standard followed specifies a masked edge correction, designated as c_{me} (Eq. 13), where d is the thickness of the specimen, b is the width of the masked edge, and S the hydraulic diameter (defined as four times the test area divided by the perimeter), all in m.

$$\Delta m_{12} = \frac{m_2 - m_1}{t_2 - t_1} \tag{12}$$

$$c_{me} = 1 + \frac{4 \bullet d}{\pi \bullet S} \ln\left(\frac{2}{1 + \exp\left(-2 \bullet \pi \bullet \frac{b}{d}\right)}\right) \tag{13}$$

Knowing the values of G and c_{me}, the exposed area of the test specimens, A, given by the arithmetic mean of the upper and lower free surfaces, in m^2, as well as the water vapour pressure difference across the specimen, Δp_v, in Pa (Eq. 15), the water vapor permeance, W, in $kg/(m^2 s Pa)$, can be calculated with Eq. (14). In Eq. 15, ϕ represents the relative humidity (dimensionless), and θ the Celsius temperature (℃).

$$W = \frac{G}{A \bullet c_{me} \bullet \Delta p_v} \tag{14}$$

$$p = \phi \bullet 610,5 \bullet e^{\frac{17,2690}{237,3+\theta}} \tag{15}$$

The δ and μ are given by Eqs. (16) and (17), respectively. Eq. (18) corresponds to the Schirmer formula and was used to calculate the water vapour permeability of the air, δ_{air}, where p_0 is the standard barometric pressure, 101325 Pa, p the barometric pressure, R_V the gas constant for water vapour, 462 Nm/(kgK), and T the thermodynamic temperature, in K.

It is also possible to determine the water vapour diffusion-equivalent air layer thickness, s_d, in m. In very permeable materials or thin membranes, the air layer between the base of the specimens and the desiccant or saturated salt solution presents some resistance to vapour flow and can therefore introduce an error in the calculations. Thus, according to the standard followed, when s_d is less than 0.2 m, the measured permeance needs to be corrected. However, as this is not the case for the material under study, which presented a low permeability, no correction for the resistance of air layers had to be applied.

Table 3
Identification of specimens and respective test conditions.

Test	Specimen	Normalised conditions (℃ – %φ)	Effective temperature (℃)	Effective relative humidity (%)	
				Climatic chamber	Cup
Wet cup	VP1 VP2 VP3	23 – 50/93	23 ± 0.3	50 ± 3	94 ± 0.6 (KNO_3)

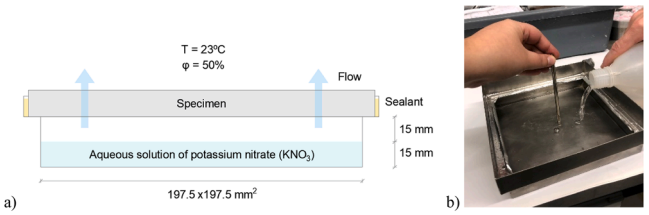

Fig. 4. Configuration of the test setup according to ISO 12572:2016 [37]: schematic drawing (a), and picture of the test procedure (b).

$$\delta = W\ d \tag{16}$$

$$\mu = \frac{\delta_{air}}{\delta} \tag{17}$$

$$\delta_{air} = \frac{0,086 p_0}{R_V T p} \left(\frac{T}{273}\right)^{1,81} \tag{18}$$

It is also possible to determine the water vapour diffusion-equivalent air layer thickness, s_d. In very permeable materials or thin membranes, the air layer between the base of the specimens and the desiccant or saturated salt solution presents some resistance to vapour flow and can therefore introduce an error in the calculations. Thus, according to the standard followed, when s_d is less than 0.2 m, the measured permeance needs to be corrected. However, as this is not the case for the material under study, which presented a low permeability, no correction for the resistance of air layers had to be applied.

4.8. Sorption isotherm

The ability of porous materials to retain moisture can lead to changes in their physical characteristics, particularly in thermal and mechanical behaviour. Hygroscopicity is very variable between different materials, as the amount of moisture retained is influenced by environmental conditions (temperature and relative humidity), material properties (porosity, pore size distribution, specific surface), and salt content [42].

Moisture fixation may result from the joint action of three fundamental mechanisms: capillarity, sorption, and condensation [43]. The sorption is due to the intermolecular forces acting on the water vapour molecules and can be divided into three phases: monomolecular sorption, multimolecular sorption and capillary condensation. While monomolecular sorption corresponds to the fixation of a layer of water molecules on the internal surface of the pores, multimolecular sorption corresponds to the fixation of several layers of molecules and occurs for higher relative humidity. Capillary condensation corresponds to the junction of the multi-molecular layers that originate the complete filling of the pores [44].

The sorption isotherm describes the relationship between the moisture content of a material and the relative humidity of the corresponding environment at a constant temperature [45], see Fig. 5. The moisture content can range between absolute zero for a relative humidity of zero, and maximum value of capillary saturation, w_{sat}, when the material is placed in contact with water in the liquid phase (capillary domain). It is also possible to reach a maximum value denominated w_{max} through humidification under pressure. The present work focuses on the hygroscopic domain, which refers to water transport predominantly in the form of water

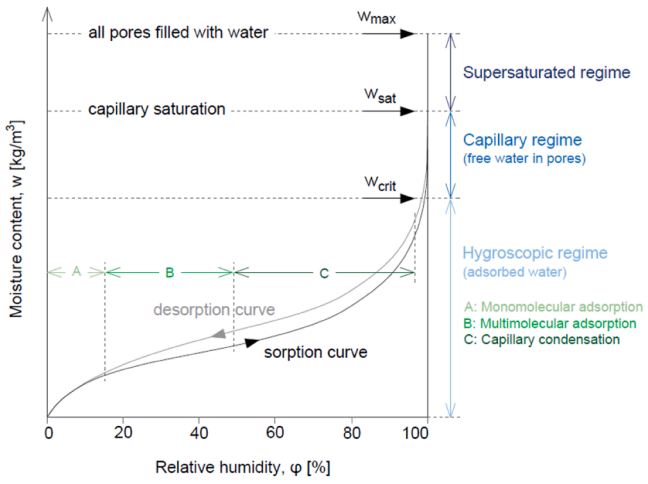

Fig. 5. Typical sorption and desorption curves (adapted from [46]).

vapour; in this domain, the maximum moisture content corresponds to the critical moisture content, w_{crit}.

The sorption isotherms of the specimens were obtained following the climatic chamber method specified in ISO 12571:2013 [38]. All specimens were dried to constant mass in a *WTB Binder* ventilated oven at a temperature of 70°C. Then, they were placed in the *Vötsch VC 4034* climatic chamber, where they were progressively exposed to different environments characterised by a constant temperature of 23 ± 0.5°C and increasing relative humidity values of 30%, 50%, 70%, 80% and 95% (Fig. 2i).

The moisture content mass by mass is determined based on Eq. (19). Where $m_{w(\varphi)}$ is the mass of the material in equilibrium with the ambience and m_0 the mass of the dry material. The moisture content mass by volume, expressed in kg/m^3, is determined by multiplying the moisture content in kg/kg by the density of the dry material in kg/m^3.

$$w(\varphi) = \frac{m_{w(\varphi)} - m_0}{m_0} \tag{19}$$

5. Analysis of experimental results

5.1. Dry bulk density, saturation moisture content and porosity

The measured dry bulk density, saturation moisture content and water absorption are presented in Table 4. From the hydrostatic weighing method, the 3D printed mortar presents an average ρ of 2059.7 ± 4.0 kg/m^3, w_{sat} of 152.5 ± 10.4 kg/m^3 and corresponding A_b of 7.4 ± 0.5%.

Cast concrete and mortars in the hardened state have typical density values from 1800 to 2400 kg/m^3 [47,48]. Also, the printable mortars in Table 6 present specific density values between 2215 and 2261 kg/m^3. The 3D printed mixture has a dry bulk density consistent with this range of values, displaying a value lower than the specific density declared by the manufacturer [27] of 2200 kg/m^3, which was expected since this value corresponds to the density of the mortar in its fresh state. The porous structure of a material impacts its density; hence high mortar density is expected to indicate low porosity associated with a compact microstructure.

Regarding the saturation moisture content, Torres [49] experimentally obtained a value of 258 kg/m^3 for a lime-based mortar with a density of 1685 kg/m^3. Compared to the w_{sat} obtained in this research, the 3D printed mortar presented, as expected, a lower value than that of the lime-based mortar.

The results of the porosity test performed are presented in Table 5, and porosity values obtained for 3D printable mortars by different authors are provided in Table 6. A porosity of 14.3% was obtained, as well as an average pore diameter of 0.0614 μm, which is similar to those presented in the mentioned studies. Fig. 6 shows the curve representing the internal porosity distribution, where an increase in the number of pores for dimensions smaller than 1 μm is clearly defined.

Porosity is affected by the type of binder, water-cement ratio (w/c), additives and admixtures, paste viscosity, and coarse aggregate size [50,51]. For the same mixture, when printed, porosity values are generally higher than cast ones (see Table 6) due to the paste's viscosity. Printed concrete has a significantly high viscosity to ensure proper flowability, buildability, and shape retention during extrusion. Also, there is no vibration or compaction of the material, which contributes to the storage of air in 3D printed specimens [52].

5.2. Specific heat capacity

The specific heat capacity results obtained for each specimen tested from 15° to 40°C are presented in.

Table 7 and Fig. 7. The evolution of the average specific heat capacity shows that a temperature of 25°C corresponds to a heat capacity of 972 $J/(kg \bullet K)$.

This indicates that a relatively large amount of heat energy is needed to increase the temperature of the mortar compared to materials with lower specific heat capacities and is in line with the values tested by Shafigh *et al.* [57], who obtained a range of values between 870 and 1040 $J/(kg \bullet K)$ for different cement mortars. Since the higher the heat capacity of a material, the better its ability to store heat, it can be assumed that the material under study will not be affected by sudden changes in temperature.

Table 4
Dry bulk density, saturation moisture content and water absorption at atmospheric pressure results.

Specimen	Dry mass m_0 (kg)	Saturated mass m_s (kg)	Immersed mass m_h (kg)	Dry bulk density ρ (kg/m^3)	Saturation moisture content w_{sat} (kg/m^3)	Water absorption A_b (%)
D1	0.64490	0.69442	0.38166	2057.8	158.0	7.68
D2	0.63891	0.68720	0.37683	2054.4	155.3	7.56
D3	0.64477	0.68991	0.37863	2067.2	144.7	7.00
D4	0.60072	0.64062	0.34938	2058.5	136.7	6.64
D5	0.61363	0.65852	0.36094	2057.9	150.5	7.32
D6	0.63252	0.68460	0.37847	2062.0	169.8	8.23
Average ± standard deviation				2059.7 ± 4.0	152.5 ± 10.4	7.4 ± 0.5

Table 6
Comparison of literature porosity results for 3D printable mortars (adapted from [52]).

Reference	Material	Density kg/m^3	Porosity (cast)	Porosity (printed)
[53]	Cement-based mortar	2261	6.8%	7.9%
[52]	Fibre-reinforced mortar (1% dosage by binder volume of polypropylene (PP) microfibres)	2222	6.5%	10.8%/10.3%[a]
[54]	Cement-based mortar	2215	–	5.0–7.0%
[55]	Cement-based mortars with different ratios of calcinated clay (M1: a blend of LGCC and HGCC with a mass ratio of 1:1, M2: mass ratio of 3:1)	–	–	M1: 14.2% M2: 8.5%
[56]	Fibre-reinforced geopolymer mortar	–	–	Without PP fibres: 10.4% 1% of PP fibre dosage: 14.1%

[a] 10.8% – cored in perpendicular direction; 10.3% – cored in longitudinal direction.

Table 5
Porosity test results.

Intruded specific volume (cm^3/g)	0.069
Average pore diameter (μm)	0.0614
Contact angle (°)	130
Surface tension of mercury (N/m)	0.049
Porosity (%)	14.3

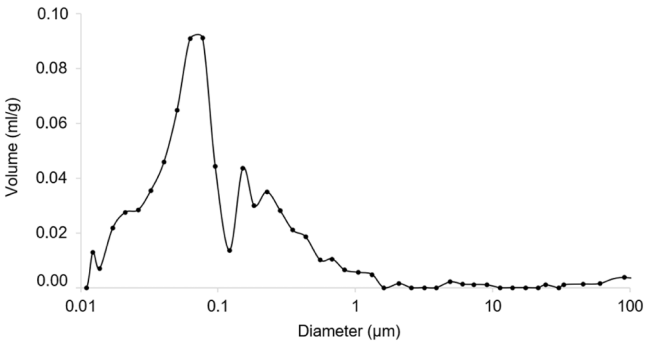

Fig. 6. Pore size distribution.

Table 7
Specific heat capacity results.

Specimen	Mass (mg)	Specific heat capacity, c_p (J/(kg • K))					
		288 K (15°C)	293 K (20°C)	298 K (25°C)	303 K (30°C)	308 K (35°C)	313 K (40°C)
HC1	51,29	921	935	950	967	987	1010
HC2	37,47	895	909	926	944	967	995
HC3	20,27	999	1018	1041	1069	1102	1139
Average ± standard deviation		938 ± 54	954 ± 57	972 ± 61	993 ± 67	1019 ± 73	1048 ± 79

5.3. Thermal conductivity

The results obtained for different moisture contents with the *Holometrix GHP-300* and *Single Specimen λ-Meter EP500e* equipment are presented in Table 8 and Table 9, respectively. Using the dry conditioning test as an example, where $\lambda_{23°C,\ dry,\ Holometrix}$ is 1.327 and $\lambda_{23°C,\ dry,\ \lambda\text{-Meter EP500e}}$ is 1.342, it can be assumed that the results obtained using the two apparatus are similar. This indicates that, although *Holometrix GHP-300* entails a more time-consuming test, the possible moisture migration within the specimens does not affect the results noticeably.

Thermal conductivity can vary depending on several factors, including composition, density, water content, aggregate type, and curing conditions. Typically, the thermal conductivity of cement-based materials falls within an extensive range, from 0.5 to 2 W/(m • K). However, the addition of supplementary cementitious materials (fly ash, silica fume), often used to enhance the properties

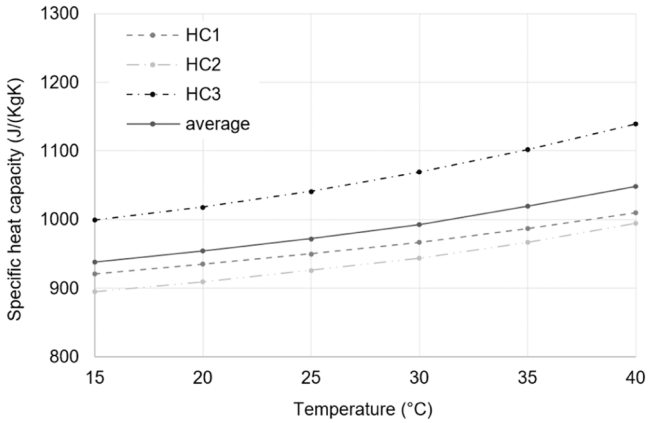

Fig. 7. Specific heat capacity curves.

Table 8
Thermal conductivity results obtained with *Holometrix GHP-300*.

Test	Specimen	23°C, dry		23°C, 50%		23°C, 80%	
		Density (kg/m^3)	λ (W/(m • K))	Density (kg/m^3)	λ (W/(m • K))	Density (kg/m^3)	λ (W/(m • K))
1	TC1	2020.70	1.308	2079.58	1.430	2100.48	1.421
	TC2	2044.34		2100.59		2128.72	
2	TC3	2010.44	1.347	2067.27	1.371	2092.06	1.515
	TC2	2044.34		2100.59		2128.72	
3	TC1	2020.70	1.325	2079.58	1.431	2100.48	1.561
	TC3	2010.44		2067.27		2092.06	
Average		2025.16	1.327	2082.48	1.411	2107.09	1.499

Table 9
Thermal conductivity results obtained with *Single Specimen λ-Meter EP500e*.

Specimen	23°C, dry		23°C, 50%		23°C, 80%	
	Density (kg/m^3)	λ (W/(m • K))	Density (kg/m^3)	λ (W/(m • K))	Density (kg/m^3)	λ (W/(m • K))
TC4	2013.69	1.379	2044.78	1.492	-	-
TC5	2011.54	1.139	2040.66	1.208	2074.57	1.232
TC6	2011.05	1.349	2045.79	1.482	2072.85	1.559
TC7	2010.98	1.397	2047.79	1.533	2076.15	1.576
TC8	1996.07	1.283	2046.02	1.463	2074.80	1.578
TC9	2020.09	1.505	2054.38	1.661	2083.12	1.710
Average	2010.57	1.342	2046.57	1.473	2076.30	1.531

and performance of 3D printed mixtures, can lower the thermal conductivity. Furthermore, mortars for 3DP have the particularity of requiring a more significant amount of fine aggregates, which can also potentially decrease their thermal conductivity.

Hence, the thermal conductivity values obtained are similar to those presented by Borges *et al.* [58] for cement-based coating mortars with different contents of fly ash, which presented $\lambda_{23°C,\ dry}$ values between 1.079 and 1.466 W/(m • K). The same can be stated when compared to the dry thermal conductivity obtained by Rocha [59], with a value of 1.173 W/(m • K) for a cement-based mortar with a density of 1877 kg/m^3 and an open porosity of 20%.

Fig. 8 presents the measured data (grey and black points) and the regression curves correlating thermal conductivity and water content (dashed lines). No strong correlations were found between moisture content (mass per mass) and thermal conductivity, which may be related to the heterogeneity that the printing process causes in the specimens.

It was observed that an increase of the relative humidity to 80% represents an increase in thermal conductivity of around 14%. This increase in moisture content was also previously reported by Gomes *et al.* [60] and Francioso *et al.* [61]. This is because water has a significantly higher thermal conductivity than air. Therefore, when moisture penetrates and fills the air pockets within the porous structure of materials, it reduces their insulating properties and increases thermal conductivity.

An increase in thermal conductivity with density was also observed, which is explained by the fact that decreasing the air voids in a material leads to an increase in its density, which is associated with lower thermal resistance.

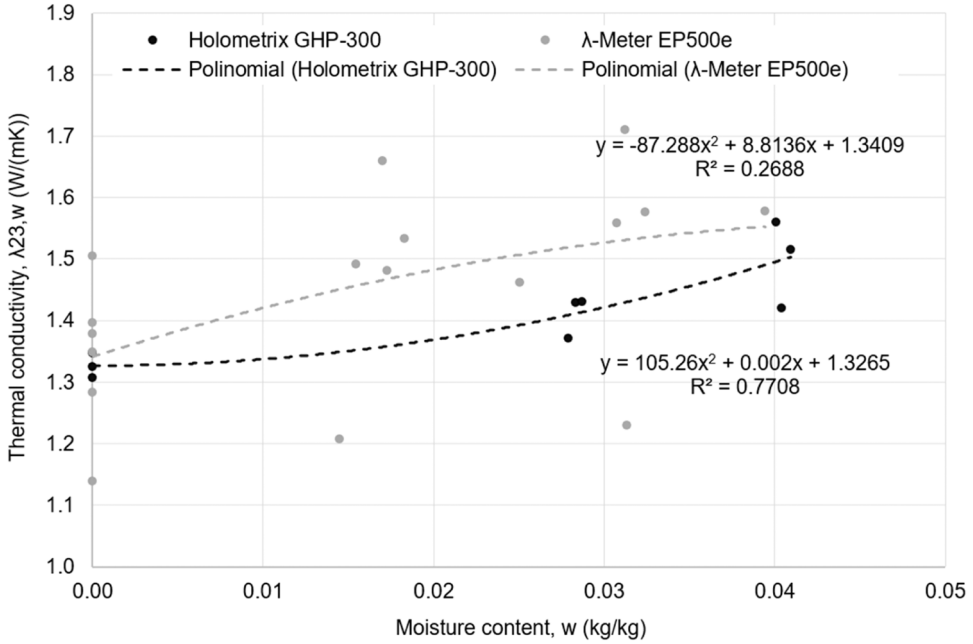

Fig. 8. Thermal conductivity at different water contents and 23ºC.

5.4. *Water absorption due to capillary action*

The results after 24 h from the start of the test are presented in Table 10. It was obtained an average A_w of 7.10×10^{-4} and 1.32×10^{-3} $kg/(m^2s^{0.5})$, depending on the orientation of the specimens. The higher A_w, the more water will be absorbed by the specimen over time; since the capillary absorption coefficient is lower than 0.2 $kg/(m^2s^{0.5})$, according to EN 998 (CEN 2017) [39], the specimens are classified as W2.

The results obtained are significantly lower than the ones obtained by Borges *et al.* [58], which ranged from 0.13 to 0.14 $kg/(m^2s^{0.5})$ for cement-based coating mortars (renders), and by Yedra *et al.* [62], from 0.05 to 0.10 $kg/(m^2s^{0.5})$ for masonry mortars. The pore structure, porosity, pore size distribution, and connectivity within the mortar influence the absorption coefficient due to capillary action. Mortars with denser microstructures, lower porosity, and smaller capillary pores exhibit lower absorption coefficients due to capillary action.

The capillary water absorption curves for the specimens tested are represented in Fig. 9. The specimens from groups 6–10, tested on the surface showing the irregularities of the deposition of the printed layers, clearly show after 10 min a higher water absorption than those from groups 1–5, which were tested in the opposite direction.

Table 10
Water absorption coefficient by capillarity results.

Specimen	Initial mass m_i (kg)	Area A (m^2)	Mass variation $\Delta m_{t=24h}$ (kg/m^2)	Absorption coefficient $A_{w,24h}$	Absorption coefficient* A_w ($kg/(m^2s^{0.5})$)
CA1	0.44538	0.0020440	0.18102	0.00062	0.00071 ± 0.000052
CA2	0.44751	0.0019986	0.21014	0.00071	
CA3	0.45324	0.0020538	0.21911	0.00075	
CA4	0.43851	0.0019984	0.22518	0.00077	
CA5	0.44498	0.0020038	0.20961	0.00071	
CA6	1.05608	0.0103632	0.36765	0.00125	0.00132 ± 0.000211
CA7	1.05989	0.0103327	0.35131	0.00120	
CA8	1.04641	0.0104140	0.38218	0.00130	
CA9	1.06518	0.0103734	0.50707	0.00173	
CA10	1.05164	0.0103022	0.33100	0.00113	

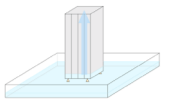

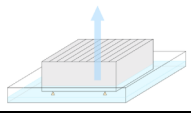

* Result presented as (average ± standard deviation)

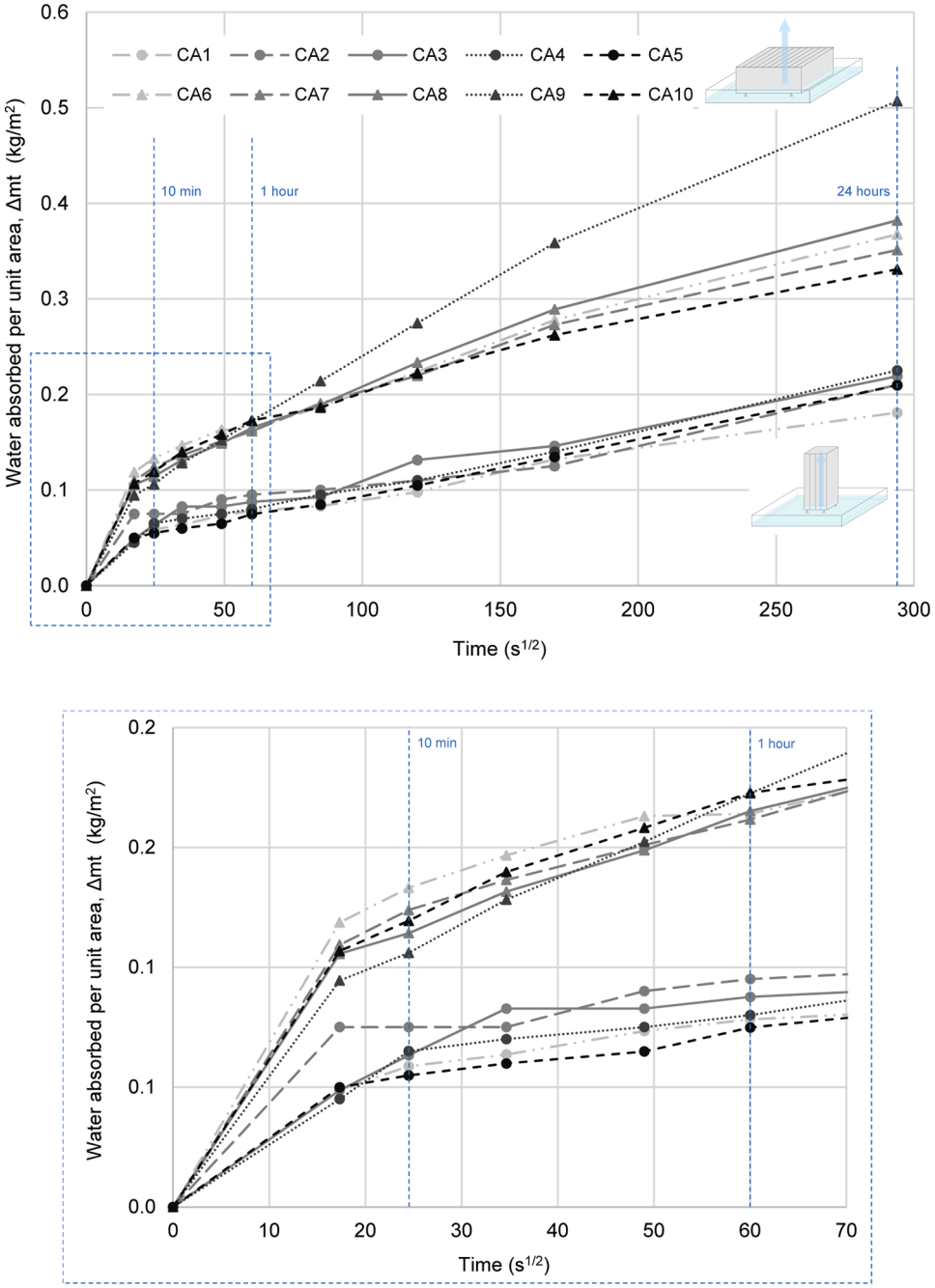

Fig. 9. Capillary absorption curves.

5.5. *Water vapour permeability*

From the results obtained for the wet cup test, presented in Table 11, it can be verified that a resistance to water vapour diffusion of 57.6 was determined.

The traditional cementitious mortars tested by Flores-Colen *et al.* [63] presented a resistance to water vapour diffusion of 18 for densities of approximately 1700 kg/m^3. The authors also state that porous materials and materials with air lime as the main binder have higher drying rates (initial drying velocities) and are the ones that presented the lower values of resistance to water vapour diffusion ($\mu < 10$).

Values of μ and δ_p presented in NIT002 [64] are: for lime and cement mortars, 15–35 and 5.3–12×10^{-12} kg/(m • s • Pa), for densities between 1800 and 1900 kg/m^3; for cementitious mortars, 15–41 and 4.5–12×10^{-12} kg/(m • s • Pa), for densities between

Table 11
Results of water vapour permeability and resistance to water vapour diffusion.

Specimen	Wet-cup (50% - 94% φ)	
	Water vapor permeability, δ_p, kg/ (m•s•Pa)	Resistance to water vapor diffusion, μ (-)
VP1	3.50×10^{-12}	57.2
VP2	3.31×10^{-12}	60.6
VP3	3.64×10^{-12}	55.0
Average*	$3.49 \times 10^{-12} \pm 1.36223 \times 10^{-13}$	57.6 ± 2.27

* Result presented as (average ± standard deviation).

1900 and 2100 kg/m^3; and for normal concrete, 110 and 1.7×10^{-12} $kg/(m \bullet s \bullet Pa)$, for a density of 2112 kg/m^3, which can vary from 15 to 260 and 0.71–13$\times 10^{-12}$ kg/(m•s•Pa), depending on the concrete density. Also, a reference value for normal concrete of 30 and 6.3×10^{-12} $kg/(m \bullet s \bullet Pa)$ is mentioned. EN 1745 [65] specifies μ values for masonry and rendering mortars between 5 and 35, for densities between 200 and 2000 kg/m^3.

The values of μ vary depending on the density of the material and its composition, and as can be inferred from the values collected from the literature, cement-based mortars and concrete can present a wide dispersion of results between 5 and 260. Considering the dry bulk density of the mortar under study (2059.7 kg/m^3, as determined in Section 5.1), it can be concluded that the values obtained are within the established range, although presenting an above-average resistance to water vapour diffusion.

A study by Silva *et al.* [66] on lime and cement mortars found a good linear correlation coefficient between porosity and water vapour diffusivity, concluding that the connectivity of porous structures has implications on water transport and mechanical properties. The larger the porous structures of the materials, the higher their water vapour permeability, which translates into a lower resistance to water vapour diffusion.

Wet cup method results are lower than dry cup method ones due to the increase in moisture transport at high relative humidity, which is explained by the contribution of liquid transport effects in hygroscopic materials [67]. Accordingly, it can be assumed that they will be higher than those for the wet cup method.

5.6. Sorption isotherm

The sorption isotherms of the printed material in equilibrium with five different relative humidity conditions, 30% (w_{30}), 50% (w_{50}), 70% (w_{70}), 80% (w_{80}) and 95% (w_{95}), are presented in Table 12. In Fig. 10, the values obtained in this study can be compared with some sorption curves found in the literature. The hygroscopic humidity for the lime-based mortar specimens was determined in a climatic chamber considering a constant temperature of 30℃ [42]. The cement-based mortar consists of Portland Cement II and sand C (volumetric ratio 1:4), has an average density of 1877 kg/m^3, an open porosity of 20%, and was submitted to a temperature of 23℃ in a climatic chamber [59]. While the sorption curve of the concrete with a density of 2300 kg/m^3 and a w/c of 0.52, determined by Hansen [45], was determined for a temperature of 20℃.

The concrete presents the most distant curve from the other three, showing the highest values in all relative humidity stages. The curve of the cement-based mortar shows a lower slope than the 3D printed mortar, where although the initial moisture content is higher for a relative humidity of around 35%, it is found to be lower for a relative humidity of 95%. This may be related to the higher open porosity of this mortar, which is 20%, whereas that of the printed mortar is 14.3%, which causes a higher initial fixation of the water molecules, which is then stabilised. The sorption isotherms of the 3D printed cement mortar and the lime mortar show a similar behaviour where the lime mortar has slower sorption up to a relative humidity of 70% and then evolves faster to reach a higher final value than the 3D printed one.

All the materials compared, which are hygroscopic, present isotherms where two distinct sections are evident in the adsorption phase. In the first section, corresponding to low moisture contents, the curve presents a smaller slope, implying that a significant increase in relative humidity results in a slight increase in the moisture content of the materials. In the second section, the curves are almost vertical, which translates into the fact that slight variations in the relative humidity of the environment generate significant

Table 12
Sorption isotherm results.

Specimen	w_{30}		w_{50}		w_{70}		w_{80}		w_{95}	
	kg/m^3	%	kg/m^3	%	kg/m^3	%	kg/m^3	%	kg/m^3	%
SI1	4.66	0.24	9.99	0.51	16.66	0.85	22.44	1.14	33.69	1.71
SI2	4.62	0.23	9.93	0.50	16.71	0.84	22.62	1.14	33.93	1.71
SI3	4.73	0.24	10.04	0.50	16.75	0.83	22.56	1.12	33.95	1.69
SI4	4.81	0.24	10.23	0.51	17.19	0.85	23.21	1.15	34.76	1.73
SI5	4.67	0.23	9.97	0.49	16.93	0.84	22.97	1.14	34.53	1.71
Average*	4.70 ± 0.07	0.24	10.03 ± 0.11	0.50	16.85 ± 0.19	0.84	22.76 ± 0.29	1.14	34.17 ± 0.40	1.71

* Result presented as (average ± standard deviation).

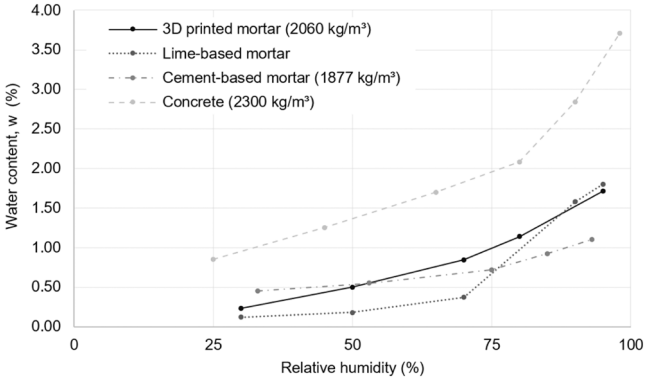

Fig. 10. Sorption isotherms of 3D printed mortar compared to other results from the literature: lime-based mortar [42], cement-based mortar [59], and concrete [45].

changes in hygroscopic humidity.

5.7. Results discussion

Table 13 summarises the experimental findings supported by a comparison with literature values for a more accessible consultation of the data obtained. An average dry bulk density of 2059.7 kg/m^3 and a specific heat capacity of 972 $J/(kg \bullet K)$ for 25℃ were obtained, values similar to those of cast concrete and traditional cementitious mortars in the construction industry. The composition (aggregate type, water content, additives) and density of materials have a strong influence on their thermal conductivity, which is why there is a typically extensive range of thermal conductivity values for cement-based materials, from 0.5 to 2 $W/(m \bullet K)$. 3DP mixtures usually include supplementary cementitious materials (such as fly ash and silica fume) and a higher proportion of fine aggregates than typical mortars, which will reduce their thermal conductivities. However, in comparison with insulating materials with average thermal conductivities lower than 0.1 $W/(m \bullet K)$ [39], the obtained value of 1.327 $W/(m \bullet K)$, for dry conditioning, marks the need for the development and analysis of suitable thermal insulation materials for 3DP. It is also important to consider the material's structure, porosity, and the nature of the interaction between moisture and its solid matrix to understand how moisture content will affect its thermal performance. In this experimental analysis, it was found that thermal conductivity increases with moisture content, which can be explained by the lower thermal conductivity of air compared to water.

Pore size and pore size distribution are important factors affecting the properties of cementitious materials, including their permeability, strength, and durability. During the hydration process of cementitious mortars, cement particles react with water, forming a hardened matrix with interconnected pores. The size of these pores varies based on the hydration level, the w/c ratio, and the presence of supplementary cementitious materials. A porosity of 14% for cementitious mortars suggests a relatively high value. Adjustments to the mix proportions and the potential use of additives or admixtures can help reduce porosity and improve mortar performance. However, in this case, a resistance to water vapour diffusion of 57.6 suggests that the cement-based mortar significantly

Table 13
Summary of the experimental results compared with literature values.

Properties		3D printed cement-based mortar		Comparison
Dry bulk density, ρ		2059.7 ± 4.0 kg/m^3		Cast concrete and mortars: from 1800 to 2400 kg/m^3 [47,48]
Saturation moisture content, w_{sat}		152.5 ± 10.4 kg/m^3		Lime-based mortar: 258 kg/m^3 (density of 1685 kg/m^3)[49]
Porosity, ε		14.3%		Cast/printed cement-based mortar: 6.8%/7.9%[53]
Specific heat capacity, c_p		972 ± 61 $J/(kg \bullet K)$ for 25℃		Cement-based mortars: 870–1040 $J/(kg \bullet K)$[57]
Thermal conductivity	λ $(W/(m \bullet K))$	*Holometrix GHP-300*	*λ-Meter EP500e*	Dry cast cement-based mortar: 1.173 $W/(m \bullet K)$ (density of 1877 kg/m^3) [59]
	dry	1.327	1.342	
	50%	1.411	1.473	
	80%	1.499	1.531	
Water absorption due to capillary action, A_w		1.32×10^{-3} $kg/(m^2 s^{0.5})$		-
Resistance to water vapour diffusion, μ		57.6 ± 2.27 (wet cup)		Cementitious mortars: 15–41 (densities 1900–2100 kg/m^3)[64]
Sorption isotherm, $w(\varphi)$	φ (%)	w (kg/m^3)		-
	30	4.70 ± 0.07		
	50	10.03 ± 0.11		
	70	16.85 ± 0.19		
	80	22.76 ± 0.29		
	95	34.17 ± 0.40		

hinders the movement of water vapour through its structure.

6. Conclusions

3D printed buildings must offer adequate insulation to ensure the desired indoor thermal environment in the same way as traditional concrete structures. In this study, a cement-based mortar was additively manufactured and experimentally characterised regarding its physical and hygrothermal properties. This experimental campaign is an important step for future research in 3DP, as it allows the analysis of hygrothermal properties essential to understand how printed cementitious materials will perform under different environmental conditions. Moreover, it ensures greater reliability when using numerical simulation software to assess heat and moisture transfer in 3D printed building elements. The following conclusions can be drawn based on this study:

- The results show that the 3D printed cement-based mortar presents poor thermal behaviour, similar to the mortars and concrete typically used in the construction industry. Thermal conductivity was shown to increase by about 14% when the relative humidity was raised to 80%. This moisture variation should be studied in more detail to assess its impact on a larger scale. Also, with the prospect of modular construction, new solutions for the thermal insulation of the connections between panels need to be addressed.
- The average pore diameter in the printed specimen was 0.0614 μm. The results show that the material exhibits a high resistance to water vapour diffusion associated with low water absorption by capillarity. This can be explained by the dimension of its pores being concentrated below 1 μm in diameter.
- Further studies should be conducted on the effect of pumping systems, fabrication constraints and durability on the hygrothermal properties of the final printed objects. Furthermore, as called for by Buswell *et al.* [68] and Wolfs *et al.* [28], the individual parameters selected during the printing process impact the final object, so it is important to highlight the need for standardisation of test methods for 3D printed materials.

Declaration of Competing Interest

The authors declare the following financial interests/personal relationships which may be considered as potential competing interests: Sofia Pessoa reports financial support was provided by Foundation for Science and Technology. Sofia Pessoa reports a relationship with Foundation for Science and Technology that includes: funding grants.

Data availability

Data will be made available on request.

Acknowledgements

This work is financed by National Funds through the FCT – Fundação para a Ciência e a Tecnologia (Portuguese Foundation for Science and Technology) within the project MIT-EXPL/TDI/0041/2019. Sofia Pessoa would like to thank FCT for financial support through the doctoral grant PD/BD/150398/2019. Finally, this work was financially supported by Base Funding - UIDB/04708/2020 of the CONSTRUCT Instituto de I&D em Estruturas e Construções - funded by national funds through the FCT/MCTES (PIDDAC).

References

[1] B. Panda, M.J. Tan, Experimental study on mix proportion and fresh properties of fly ash based geopolymer for 3D concrete printing, (in English), Ceram. Int. vol. 44 (9) (2018) 10258–10265.
[2] B. Panda, C. Unluer, M.J. Tan, Investigation of the rheology and strength of geopolymer mixtures for extrusion-based 3D printing, Cem. Concr. Compos. vol. 94 (2018) 307–314.
[3] M. Valente, M. Sambucci, M. Chougan, S.H. Ghaffar, Composite alkali-activated materials with waste tire rubber designed for additive manufacturing: an eco-sustainable and energy saving approach, J. Mater. Res. Technol. vol. 24 (2023) 3098–3117.
[4] M. Chougan, et al., Effect of natural and calcined halloysite clay minerals as low-cost additives on the performance of 3D-printed alkali-activated materials, Mater. Des. vol. 223 (2022).
[5] F. Hamidi, F. Aslani, Additive manufacturing of cementitious composites: materials, methods, potentials, and challenges, Constr. Build. Mater. vol. 218 (2019) 582–609, 2019/09/10/.
[6] H. Jeong, S.-J. Han, S.-H. Choi, Y.J. Lee, S.T. Yi, K.S. Kim, Rheological property criteria for buildable 3D printing concrete, Materials vol. 12 (4) (2019) 657.
[7] Z. Pan, D. Si, J. Tao, J. Xiao, Compressive behavior of 3D printed concrete with different printing paths and concrete ages, Case Stud. Constr. Mater. vol. 18 (2023).
[8] P. Shakor, S. Nejadi, G. Paul, A study into the effect of different nozzles shapes and fibre-reinforcement in 3D printed mortar, Materials (Basel) vol. 12 (10) (2019). May 26.
[9] P. Shakor, S. Nejadi, S. Sutjipto, G. Paul, N. Gowripalan, Effects of deposition velocity in the presence/absence of E6-glass fibre on extrusion-based 3D printed mortar, Addit. Manuf. vol. 32 (2020).
[10] M. Mathi, M.C. Sundarraja, R. Shanthipriya, A comparative study of the thermal comfort of different building materials in Madurai, Int. J. Earth Sci. Eng. vol. 7 (2014) 1004–1018.
[11] N. Khamporn, S. Chaiaypinunt, An investigation on the human thermal comfort from a glass window, Eng. J. vol. 18 (2014) 25–43.
[12] R. De Lieto Vollaro, C. Guattari, L. Evangelisti, G. Battista, E. Carnielo, P. Gori, Building energy performance analysis: a case study, Energy Build. vol. 87 (2014) 87–94.
[13] B. Rodríguez Soria, J. Hernández, J. Pérez-Bella, J.J. Díaz, Quantitative analysis of the divergence in energy losses allowed through building envelopes, Renew. Sustain. Energy Rev. vol. 49 (2015) 1000–1008.

[14] J. Sun, J. Xiao, Z. Li, X. Feng, Experimental study on the thermal performance of a 3D printed concrete prototype building, Energy Build. vol. 241 (2021).
[15] S. Pessoa, A.S. Guimarães, S.S. Lucas, N. Simões, 3D printing in the construction industry - a systematic review of the thermal performance in buildings, Renew. Sustain. Energy Rev. vol. 141 (2021), 110794.
[16] N. Gama, A. Ferreira, A. Barros-Timmons, 3D printed cork/polyurethane composite foams, Mater. Des. vol. 179 (2019).
[17] K. Cuevas, M. Chougan, F. Martin, S.H. Ghaffar, D. Stephan, P. Sikora, 3D printable lightweight cementitious composites with incorporated waste glass aggregates and expanded microspheres – Rheological, thermal and mechanical properties, J. Build. Eng. vol. 44 (2021).
[18] V.V. Molodin, E.V. Vasenkov, P.L. Timin, Work head for 3D printing of insulated walls from one-stage polystyrene concrete, Mater. Sci. Forum vol. 992 (2020) 194–199.
[19] M. Sambucci, M. Valente, Thermal insulation performance optimization of hollow bricks made up of 3D printable rubber-cement mortars: material properties and FEM-based modelling, IOP Conf. Ser.: Mater. Sci. Eng. vol. 1044 (1) (2021).
[20] V. Markin, M. Krause, J. Otto, C. Schröfl, V. Mechtcherine, 3D-printing with foam concrete: From material design and testing to application and sustainability, J. Build. Eng. vol. 43 (2021).
[21] H. Alghamdi, N. Neithalath, Synthesis and characterization of 3D printable geopolymeric foams for thermally efficient building envelope materials, Cem. Concr. Compos. vol. 104 (2019).
[22] D. Chaiyotha, W. Kantawong, P. Payakaniti, S. Pinitsoontorn, P. Chindaprasirt, Finding optimized conditions for 3D printed high calcium fly ash based alkali-activated mortar, Case Stud. Constr. Mater. vol. 18 (2023).
[23] S. Pessoa, M. Jesus, A. Guimarães, S. Lucas, N. Simões, Upcoming challenges on the application of thermal insulation in 3D printed building elements, CEES International Conference Proceedings, 2021.
[24] TU/e. (2021). First resident of 3D-printed concrete house in Eindhoven receives key. Available: https://www.tue.nl/en/news-and-events/news-overview/30–04-2021-first-resident-of-3d-printed-concrete-house-in-eindhoven-receives-key/ (accessed on 28 January 2022).
[25] M. Posani, R. Veiga, V.P. de Freitas, Thermal mortar-based insulation solutions for historic walls: An extensive hygrothermal characterization of materials and systems, Constr. Build. Mater. vol. 315 (2022).
[26] M. Maaroufi, R. Belarbi, K. Abahri, F. Benmahiddine, Full characterization of hygrothermal, mechanical and morphological properties of a recycled expanded polystyrene-based mortar, Constr. Build. Mater. vol. 301 (2021).
[27] S.-G.W. Beamix. (2021). Weber 3D 160–1 and Weber 3D 145–2. Available: https://www.3d.weber/materials/ (accessed on 4 July 2022).
[28] R.J.M. Wolfs, F.P. Bos, T.A.M. Salet, Hardened properties of 3D printed concrete: The influence of process parameters on interlayer adhesion, (in English), Cem. Concr. Res. vol. 119 (2019) 132–140 (May).
[29] F. Bos, R. Wolfs, Z. Ahmed, T. Salet, Additive Manufacturing of Concrete in Construction: Potentials and Challenges of 3D Concrete Printing, Virtual Phys. Prototyp. vol. 11 (3) (2016) 209–225.
[30] ISO/TC 261/JG 80. Available: https://standards.iteh.ai/catalog/tc/iso/39061f43–0796-4895-bb74-a2e58f6949f5/iso-tc-261-jg-80 (accessed on 18 December 2021).
[31] EN, EN 1015 Methods of test for mortar for masonry. Part 10: Determination of dry bulk density of hardened mortar, European Committee for Standardization,, *Brussels*, 1999.
[32] BS 2008. BS EN 13755. Natural stone test methods. Determination of water absorption at atmospheric pressure: British Standard.
[33] ISO. 2016. ISO 15901–1 Evaluation of pore size distribution and porosity of solid materials by mercury porosimetry and gas adsorption. Part 1: Mercury porosimetry: International Standard.
[34] ASTM. 2018. ASTM E1269–11. Standard test method for determining specific heat capacity by differential scanning calorimetry: International Standard.
[35] EN, EN 12664 Thermal performance of building materials and products. Determination of thermal resistance by means of guarded hot plate and heat flow meter methods. Dry and moist products of medium and low thermal resistance, European Committee for Standardization, Brussels, 2001.
[36] ISO. 2002. ISO 15148 Hygrothermal performance of building materials and products. Determination of water absorption coefficient by partial immersion: International Standard.
[37] ISO. 2016. ISO 12572 Hygrothermal performance of building materials and products. Determination of water vapour transmission properties. Cup method: International Standard.
[38] ISO. 2013. ISO 12571 Hygrothermal performance of building materials and products. Determination of hygroscopic sorption properties: International Standard.
[39] CEN, EN 998 Specification for mortar for masonry. Part 1: Rendering and plastering mortar, European Commitee for Standardization,, *Brussels*, 2017.
[40] ISO. 2000. ISO 12570 Hygrothermal performance of building materials and products. Determination of moisture content by drying at elevated temperature: International Standard.
[41] ISO. 1991. ISO 8302 Thermal insulation. Determination of steady-state thermal resistance and related properties. Guarded hot plate apparatus: International Standard.
[42] LNEC, Characterization of the hygroscopicity of lime-based mortars, in Report 201/2007 – NRI, Lisbon, Portugal 2007, Available: http://repositorio.lnec.pt:8080/jspui/handle/123456789/16056.
[43] A.S. Guimarães, Experimental characterisation of the operation of base-wall ventilation systems for the treatment of rising damp, Master thesis, Faculty of Engineering of the University of Porto, Porto, Portugal 2007.
[44] N. Ramos, The importance of hygroscopic inertia in the hygrothermal behaviour of buildings, Doctoral thesis, Faculty of Engineering of the University of Porto, Porto, Portugal 2007.
[45] K.K. Hansen, Sorption isotherms: A catalogue, Byg Rapport No. TR162, Technical University of Denmark, 1986.
[46] J. Straube, J. Smegal, Modeled and Measured Drainage, Storage and Drying Behind Cladding Systems, presented at the ASHRAE Thermal Performance of the Exterior Envelopes of Whole Buildings International Conference, Florida, 2007.
[47] ISO. 2007. ISO 10456 Building materials and products. Hygrothermal properties. Tabulated design values and procedures for determining declared and design thermal values: International Standard.
[48] LNEC. 2006. ITE 50 Thermal Transmittance Coefficients of Elements of the Buildings Envelope (in Portuguese).
[49] I. Torres, Rising damp in walls of historic buildings, Doctoral thesis, Coimbra, 2004.
[50] P.C. Aïtcin, Entrained air in concrete: rheology and freezing resistance, Science and Technology of Concrete Admixtures (2016) 87–95.
[51] R. Kumara, B. Bhattacharjeeb, Porosity, pore size distribution and in situ strength of concrete, Cem. Concr. Res. vol. 33 (2003) 155–164.
[52] M. van den Heever, A. du Plessis, J. Kruger, G. van Zijl, Evaluating the effects of porosity on the mechanical properties of extrusion-based 3D printed concrete, Cem. Concr. Res. vol. 153 (2022).
[53] J. Kruger, A. du Plessis, G. van Zijl, An investigation into the porosity of extrusion-based 3D printed concrete, Addit. Manuf. vol. 37 (2021).
[54] H. Lee, J.-H.J. Kim, J.-H. Moon, W.-W. Kim, E.-A. Seo, Correlation between pore characteristics and tensile bond strength of additive manufactured mortar using X-ray computed tomography, Constr. Build. Mater. vol. 226 (2019) 712–720.
[55] Y. Chen, O. Çopuroğlu, C. Romero Rodriguez, F.F. d Mendonca Filho, E. Schlangen, Characterization of air-void systems in 3D printed cementitious materials using optical image scanning and X-ray computed tomography, Mater. Charact. vol. 173 (2021).
[56] B. Nematollahi, et al., Effect of polypropylene fibre addition on properties of geopolymers made by 3D printing for digital construction, Materials vol. 11 (12) (2018). Art. no. 2352.
[57] P. Shafigh, I. Asadi, A.R. Akhiani, N.B. Mahyuddin, M. Hashemi, Thermal properties of cement mortar with different mix proportions, Mater. De. Constr. vol. 70 (339) (2020).
[58] A. Borges, I. Flores-Colen, J. de Brito, Physical and mechanical performance of cement-based renders with different contents of fly ash, expanded cork granules and expanded clay, Constr. Build. Mater. vol. 191 (2018) 535–543.
[59] D. Rocha, Analysis of the potential for using hygroscopic inertia in buildings, Master thesis, Universidade Nova de Lisboa, Lisbon, Portugal 2016.

[60] M.G. Gomes, I. Flores-Colen, L.M. Manga, A. Soares, J. de Brito, The influence of moisture content on the thermal conductivity of external thermal mortars, Constr. Build. Mater. vol. 135 (2017) 279–286.
[61] V. Francioso, C. Moro, M. Velay-Lizancos, Effect of recycled concrete aggregate (RCA) on mortar's thermal conductivity susceptibility to variations of moisture content and ambient temperature, J. Build. Eng. vol. 43 (2021).
[62] E. Yedra, D. Ferrández, C. Morón, P. Saiz, New test methods to determine water absorption by capillarity. Experimental study in masonry mortars, Constr. Build. Mater. vol. 319 (2022).
[63] I. Flores-Colen, L. Silva, J. de Brito, V.P. de Freitas, Drying index for in-service physical performance assessment of renders, Constr. Build. Mater. vol. 112 (2016) 1101–1109.
[64] V. Freitas, P. Pinto, Technical Information NIT 002. Vapour permeability of building material: internal condensation, LFC, Laboratory of Building Physics, Portugal (in Portuguese), 1998.
[65] EN, EN 1745 Masonry and masonry products. Methods for determining thermal properties, European Committee for Standardization,, *Brussels*, 2000.
[66] B.A. Silva, A.P. Ferreira Pinto, A. Gomes, Natural hydraulic lime versus cement for blended lime mortars for restoration works, Constr. Build. Mater. vol. 94 (2015) 346–360.
[67] H.M. Künzel, Simultaneous heat and moisture transport in building components: One- and two-dimensional calculation using simple parameters, Fraunhofer Institute of Building Physics, Fraunhofer IRB Verlag Stutgart, 1995.
[68] R.A. Buswell, W.R.L. de Silva, S.Z. Jones, J. Dirrenberger, 3D printing using concrete extrusion: A roadmap for research, Cem. Concr. Res. vol. 112 (2018) 37–49.